TiO$_2$/graphene and TiO$_2$/graphene oxide nanocomposites for photocatalytic applications: A computer modeling and experimental study

P.M. Martins [a,b,*,1], C.G. Ferreira [a,1], A.R. Silva [a,b], B. Magalhães [a], M.M. Alves [b], L. Pereira [b], P.A.A.P. Marques [c], M. Melle-Franco [d,e], S. Lanceros-Méndez [a,f,g,*]

[a] Center of Physics, University of Minho, 4710-057 Braga, Portugal
[b] Center of Biological Engineering, University of Minho, 4710-057 Braga, Portugal
[c] TEMA/Department of Mechanical Engineering, University of Aveiro, 3810-193 Aveiro, Portugal
[d] CICECO, Aveiro Institute of Materials, Department of Chemistry, University of Aveiro, 3810-193 Aveiro, Portugal
[e] ALGORITMI Center, Department of Informatics, University of Minho, 4710-057 Braga, Portugal
[f] BCMaterials, Basque Center for Materials, Applications and Nanostructures, UPV/EHU Science Park, 48940 Leioa, Spain
[g] IKERBASQUE, Basque Foundation for Science, 48013 Bilbao, Spain

A B S T R A C T

This work reports a computational study, focused on graphene (G) and graphene oxide (GO) interfaces with titanium dioxide (TiO$_2$), and an experimental assay on the photocatalytic activity of TiO$_2$/G and TiO$_2$/GO nanocomposites in the degradation of two different pollutants: methylene blue and ciprofloxacin. Both carbon nanostructures were compared due to their different chemical structure: GO is a G derivative with oxygen functional groups which should promote a closer chemical interaction with TiO$_2$ nanoparticles. Computational models of the fundamental properties of the composites indicated potentially improved photocatalytic activity compared to TiO$_2$, namely lower band gaps and charge carrier segregation at the interfaces. These fundamental properties match qualitatively experimental results on methylene blue, which was more effectively degraded by TiO$_2$/G and TiO$_2$/GO nanocomposites than by pure TiO$_2$ under UV light. In contrast, the same nanocomposites were found to be less efficient to degrade ciprofloxacin than pure TiO$_2$ under visible and UV light. Therefore, this work showcases the relevance of an efficient matching between the catalyst and the molecular properties and structure of the pollutant.

1. Introduction

Water contamination is one of the most serious environmental issues, as many hazardous micropollutants, such as heavy metals, pharmaceuticals, dyes, fertilizers, and pesticides are increasingly being released into the watercourses [1–3]. Since these pollutants present high toxicities and thus constitute a threat to fauna and flora, it is essential to develop efficient techniques for water decontamination [4,5].

Semiconductor-based heterogeneous photocatalysis is one of the most promising processes for the treatment of contaminated water. Among the available catalysts, titanium dioxide (TiO$_2$) presents the most suitable properties: it is chemically and biologically inert, stable, non-toxic, cheap and easy to produce [6,7]. However, it has an energy band gap (3.2 eV for the anatase phase and 3.0 eV for the rutile phase) with photoexcitation in the ultraviolet (UV) range. This translates to a reduced spectral activation with natural light since UV radiation

corresponds to just 5% of the solar spectrum.[4] Further, the recombination of photogenerated electron-hole pairs is high, which results in reduced photocatalytic efficiency [4,8].

Several strategies have been attempted to tailor TiO$_2$'s band gap and to reduce the electron-hole recombination to overcome these limitations, namely doping TiO$_2$ with metallic [9], no-metallic [10], and rare earth elements [4], and mixing TiO$_2$ with other nanomaterials [8]. One particularly promising approach lies on the mixing with graphene (G) and graphene oxide (GO) to develop TiO$_2$ nanocomposites (designated by TiO$_2$/G and TiO$_2$/GO, respectively), as these composite materials have been found to present improved electronic and optical properties for photocatalysis.

TiO$_2$/G and TiO$_2$/GO nanocomposites have been produced by solvothermal [11], hydrothermal [12,13] and one-step colloidal blending [14] methods. These nanocomposites have been assessed for the degradation of pollutants, namely: methylene blue (under UV and visible-

---

light irradiation) [12,14], risperidone (using artificial sunlight and visible radiation) [13], naphthenic acids [11] methyl orange and dimethyl phthalate [15] (both under UV irradiation). In these studies, high photocatalytic efficiency was found which was attributed to increasing adsorption of the pollutants onto the nanoparticles surface and to increased separation of charge carriers, which effectively inhibits recombination. Computationally, DFT studies regarding the electronic properties of TiO_2/G interfaces have been reported addressing the interfaces of TiO_2 surfaces/slabs for the anatase [16,17] and rutile crystal phases [18] with one graphene adlayer. In all these studies, it was found that these interfaces show a reduced band gap and at the same time promote separation of charge carriers at the interfaces.

Few of the reported works to date relate the photocatalytic efficiency with the G/GO concentration, and none of them compares the performance of the TiO_2/G with the performance of the TiO_2/GO nanocomposites. Further, although the properties of TiO_2/G interfaces have been computationally calculated previously, the properties of TiO_2/GO interfaces are yet to be determined.

Therefore, the present work comprises a complementary computational and experimental investigation of the photocatalytic activity of TiO_2/G and TiO_2/GO nanocomposites with different contents of graphene and GO. These nanocomposites were used to degrade a dye (methylene blue - MB) and an antibiotic (ciprofloxacin – CIP), under UV and visible-light irradiation, to evaluate and compare their photocatalytic performance. Moreover, this is, to the best of our knowledge, the first study that uses these nanocomposites to degrade antibiotics, even though these represent a serious concern to the environment due to their toxicity and the increased risk of new antibiotic-resistant microorganisms [3]. Also, the fundamental electronic properties of TiO_2/ G and TiO_2/GO interfaces were also computed through density functional tight-binding method to rationalize the results.

2. Experimental methods

2.1. Computer model

Computations were performed with Self Consistent Charge Density Functional Tight Binding (SCC-DFTB) Hamiltonian, with the *tiorg* parameters set, using the software *DFTB+* (version 1.2.2) [19]. The DFTB Hamiltonian shows a higher computational efficiency than DFT methods and therefore is ideal for the study of large systems [20,21].

The structure and electronic properties of the pristine materials and the TiO_2/G and TiO_2/GO interfaces were computed and compared. Interfaces between TiO_2 surface slabs and graphene/GO sheets were built using *Virtual NanoLab* software (version 2015.1) from *QuantumWise*. For the TiO_2 slabs, the most thermodynamically stable surfaces of anatase (101) and rutile (110) were computed with two atomic layers. Suitable commensurate graphene and GO layers were cut and interfaced with the slabs. For simplicity, the GO model considered in this study assumed a full, two face, functionalization of the graphene with epoxy C-O functional groups with a ratio C:O of 2. Interfaces of anatase/graphene (A/G), rutile/graphene (R/G), anatase/GO (A/GO) and rutile/GO (R/GO) were studied. The number of atoms contained in TiO_2 slabs and graphene/GO layers, as well as the commensurate supercell dimensions and strains of the interfaces, are listed in Table 1.

For all cases, a vacuum slab of approximately 15 Å perpendicular to the interface was considered. The use of the DFTB Hamiltonian allowed the modeling of a larger system than those reported in the literature [16–18] with lower strain values, *i.e.,* higher commensurability.

Geometry optimization of the interfaces was performed through the conjugate gradient method, considering a maximum force of 10^{-4} Ha/ Bohr. The atoms of the bottom layer of the TiO_2 slab were fixed at the bulk positions. Two different Monkhorst-Pack meshes were used, one for the geometry optimization and a denser one to compute the electronic properties and the adhesion energy. The charge transfer isosurfaces were computed with the *waveplot* software (version 0.3.1). Details of the meshes used are presented in the supplementary information.

3. Materials

TiO_2 (P25 - AEROXIDE) nanoparticles (kindly provided by Evonik Industries®). Graphite flakes (99.99%) and all the remaining chemicals were supplied by Sigma-Aldrich and used as received. The water used in all the photocatalytic experiments is ultra-pure (Millipore).

3.1. Preparation of TiO_2/G and TiO_2/GO nanocomposites

Graphene oxide (GO) was produced by the chemical exfoliation of graphite flakes, according to the method suggested by Hummers and Offeman [22,23]. Briefly, 7 g of $KMnO_4$ was added to a suspension containing 50 mL of concentrated H_2SO_4 and 2 g of graphite. The resulting mixture was magnetically stirred for 2 h and then treated with a solution of H_2O_2 (30 wt % in water) until the gas evolution ceased. After that, the suspension was intensively washed, first with a diluted solution of HCl (0.1 mol/dm^3) and then with distilled water by filtration. Finally, the solution was centrifuged and dried by lyophilization to obtain the GO. The quality of the GO flakes was evaluated by AFM, Raman and SEM characterization (data not shown).

The graphene was obtained from the reduction of the GO, by adding 2 mL of NH_2OH (0.1 mol/dm^3) to 10 mL of a suspension of GO (0.5 mg/ mL). After stirring for 30 min, the pH was adjusted to 12 by adding an aqueous solution of NaOH (0.1 mol/dm^3). Then the suspension was heated to 80 °C for 1 h and finally washed by centrifugation. The success of the GO flakes reduction was accessed by Raman spectroscopy (data not shown).

The synthesis of the TiO_2/G and TiO_2/GO nanocomposites was based on a one-step hydrothermal method described in previous studies [8,12]. In short, the appropriate amount of graphene/GO (depending on the wt % of the composites required – namely 0.5%, 1%, 1.5% and 3%) was dispersed in a mixture of 40 mL of deionized water and 20 mL of ethanol and stirred by ultrasonication for 1 h. Subsequently, 100 mg of TiO_2 were added, and the resulting suspension was stirred for 2 h to achieve a complete homogenization. After that, 15 mL of this suspension was placed in a Teflon lined autoclave, sealed and heated to 120 °C during 3 h. The resulting nanocomposites were then washed with deionized water and freeze-dried to avoid the agglomeration of the particles.

4. Materials characterization

Scanning electron microscopy (SEM) characterization was performed with an FEI *Quanta 650 FEG* microscope, equipped with an *INCA 350* spectrometer from *Oxford Instruments* for energy dispersive X-ray spectroscopy (EDX). A small amount of powder was placed in copper tape and observed under 20 kV.

To identify the vibrational modes of the nanocomposites, Fourier transform infrared spectroscopy (FTIR) was performed in attenuated total reflectance (ATR) mode, using a *PerkinElmer Spectrum Two IR* Spectrometer and considering 64 scans, with a resolution of 4 cm^{-1}.

Diffuse reflectance spectroscopy (DRS) was performed by a

Table 1
Number of atoms, supercell dimensions and strain, considered in the construction of the interfaces.

Interface	TiO_2 atoms	G/GO atoms	Supercell dimensions	Strain
A/G	240	144	$51.48 \times 7.43 \times 35$ Å^3	0.80%
R/G	360	224	$30.03 \times 19.82 \times 35$ Å^3	0.11%
A/GO	312	264 (176 C)	$10.36 \times 49.33 \times 35$ Å^3	0.42%
R/GO	252	216 (144 C)	$46.60 \times 8.97 \times 35$ Å^3	0.80%

Shimadzu UV-2501 PC apparatus equipped with integrating spheres. These measurements allowed to estimate the band gap of the photocatalysts, by converting the reflectance spectra to absorption Kubelka-Munk units through equation (1) [24]:

$$F(R_\infty) = \frac{(1 - R_\infty)^2}{2R_\infty} \qquad (1)$$

where $F(R_\infty)$ is the Kubelka-Munk function and R_∞ is the absolute diffuse reflectance.

The crystallinity of the samples was accessed through X-ray diffraction (XRD) using a *Philips PW 1710* diffractometer with a Cu source (K_α, λ = 1.5045 Å) operating at 40 kV and 30 mA, at room temperature.

The specific surface area, pore volume, and pore size were assessed by BET (Brunauer–Emmett–Teller) using a Micromeritics Instrument Corp. (Gemini V2.00).

4.1. Photocatalytic experiments

The photocatalytic activity of TiO_2 composites with different G and GO content were evaluated through the degradation of methylene blue (MB) and ciprofloxacin (CIP) aqueous solutions (0.015 mmol/l) at pH ~ 4, under UV and visible light. For this, 50 mg of the catalysts were added to 50 mL of solution and magnetically stirred in the dark for 30 min, to achieve the adsorption-desorption equilibrium. Afterward, the UV photocatalytic degradations were carried out using a home-made photoreactor equipped with six *8W mercurial fluorescent* lamps, from *Philips*, with a flux of 1.6–1.7 mW/cm^2 and an excitation peak of 365 nm, placed at 10 cm above the solution. For the visible light experiments, an *Ingenieurburo Mencke & Tegtmeyer GmbH* sun simulator, with a flux of 9.8 mW/cm^2, was used. In this case, the light source was placed 21 cm above the solution.

For both the experimental setups, the reaction rate and efficiency of the degradation were determined by monitoring the intensity of the main absorbance peaks of MB (664 nm) and CIP (276 nm), using a *Biotek Cytation3* spectrophotometer. The experiments revealed that the degradation of both solutions fitted to a pseudo-first-order reaction, Langmuir–Hinshelwood model, expressed by equation (2): [25].

$$\ln \frac{C}{C_0} = -kt \qquad (2)$$

where C_0 and C represent the concentration of the pollutant at time 0 min and at time t, respectively, and k is the first-order rate constant of the reaction.

5. Results

5.1. Computational modeling

Modelled structures of the interfaces A/G and A/GO are presented in Fig. 1a and Fig. 1d, respectively, while for the R/G and R/GO interfaces the structures obtained are shown in the supporting information. Equilibrium distances measured between the top of the TiO_2 slabs and the graphene/GO layers are listed in Table 2. These distances ranged between 2.53 Å, for the A/GO interface, and 2.92 Å, for the R/GO one.

The interfacial adhesion energy, defined as the difference between the total energy of the interface and the sum of the energies of the TiO_2 slab and the graphene/GO layer, was calculated for all systems. The values obtained, per carbon atom, are also presented in Table 2. For all the interfaces, the adhesion energy was negative, which indicates that these are thermodynamically stable. Adhesion energies were three/four times larger for the TiO_2/G interfaces than for the TiO_2/GO ones, which is mostly because graphene layers are perfectly flat and, therefore, TiO_2/G interfaces should be more stable thermodynamically.

The density of States (DOS) were computed in the optimized geometries, to characterize the electronic structure of the interfaces, and are presented in Fig. 1b and e, for the A/G and A/GO systems, and in the supporting information. In both cases, the presence of the graphene/GO leads to significant changes in the DOS of the composites, with the introduction of new energy states inside the band gap of TiO_2. For the A/G interface, the energy gap, calculated as the energy difference between the lowest unoccupied orbital and the highest occupied orbital, is null as the graphene Fermi Energy matches the upper valence band of TiO_2. This band is composed mainly of O 2p and Ti 3d states of the TiO_2, whereas the lower conduction band consists of delocalized C 2p states of the graphene. Analogous results were also obtained for the R/G interface. On the other hand, the A/GO interface has a band gap of 1.79 eV, and in this case, the transitions are expected to occur from the O 2p and Ti 3d states of the TiO_2 to the C 2p and O 2p states of the GO. These results were similar to the obtained for the interface R/GO, with a lower gap of 1.31 eV.

Charge density difference maps of the interfaces A/G and A/GO are presented in Fig. 1c and f, respectively (charge density maps for the different interfaces are shown as supplementary material – Table 1). Additionally, in supplementary material, Fig. S1 illustrates the Optimized geometries, the density of states and charge density differences of all the materials interfaces (Anatase/G, Rutile/G, Anatase/GO and Rutile/GO). The blue isosurfaces correspond to regions of charge accumulation, while the yellow isosurfaces represent spaces of charge depletion. For all interfaces, separation of charge carriers was observed, with an accumulation of electrons in the TiO_2 slab and of holes in the graphene/GO layers. The average charge transfer per adlayer atom to the TiO_2 surface slabs, for all the interfaces constructed, are listed in Table 2. The calculated values ranged between 8×10^{-7} e/atom, for the R/GO interface, and 7×10^{-4} e/atom, for the A/G one.

6. Materials characterization

SEM analysis of the samples TiO_2, TiO_2/G 1%, 3% and TiO_2/GO 1%, 3% was performed. The results obtained for the nanocomposites with 3% of graphene and GO are presented in Fig. 2. These images show the presence of TiO_2 agglomerates, and due to the high amount of TiO_2 compared with the carbon nanosheets, the latter are less visible. Also, it is expected that during the hydrothermal treatment the TiO_2 nanoparticles completely adhere to their surfaces. Even so, it is also possible to identify some GO sheets for the TiO_2/GO 3% composite, amplified in the upper right corner of Fig. 2b.

The elemental composition of the TiO_2/G 3% and TiO_2/GO 3% nanocomposites was determined by EDX. The results, shown in Fig. 3a, allowed to identify the presence of carbon (C), oxygen (O) and titanium (Ti), which can all be addressed to the nanocomposites.

XRD was performed to access their crystalline properties. Diffractograms obtained for pure TiO_2, TiO_2/G 3%, and TiO_2/GO 3% nanocomposites are shown in Fig. 3b. The diffraction peaks observed are appropriately identified. All of them correspond to the characteristic TiO_2 crystal planes, in both anatase, A, (25°, 38°, and 48° peaks) and rutile, R, (the 27° peak) crystal phases (JCPDS cards 21–1272 and 21–1276, respectively [26]). The expected peaks of graphene (23°-24°) or GO (7°-12°) were not found [27], probably due to their low concentration in the composites. Using *Match* software (version 1.10b), the weight ratio of anatase and rutile phases was estimated from XRD spectra. The results, listed in Table 3, indicate that the initial TiO_2 powder is composed of roughly 80% anatase and 20% rutile (in good agreement with the specifications values of the Aeroxide P25 particles. The produced nanocomposites present an anatase content ranging from 73.8% to 77.2% and a rutile content ranging between ≈23% and 26%.

FTIR-ATR measurements were performed to assess the chemical interactions within the composites. The spectra obtained for the TiO_2, TiO_2/G 3%, and TiO_2/GO 3% samples are shown in Fig. 3c. The most prominent absorption bands observed correspond to water O-H stretching modes (at 3350 cm^{-1} and 1640 cm^{-1}) and Ti-O-Ti bonds
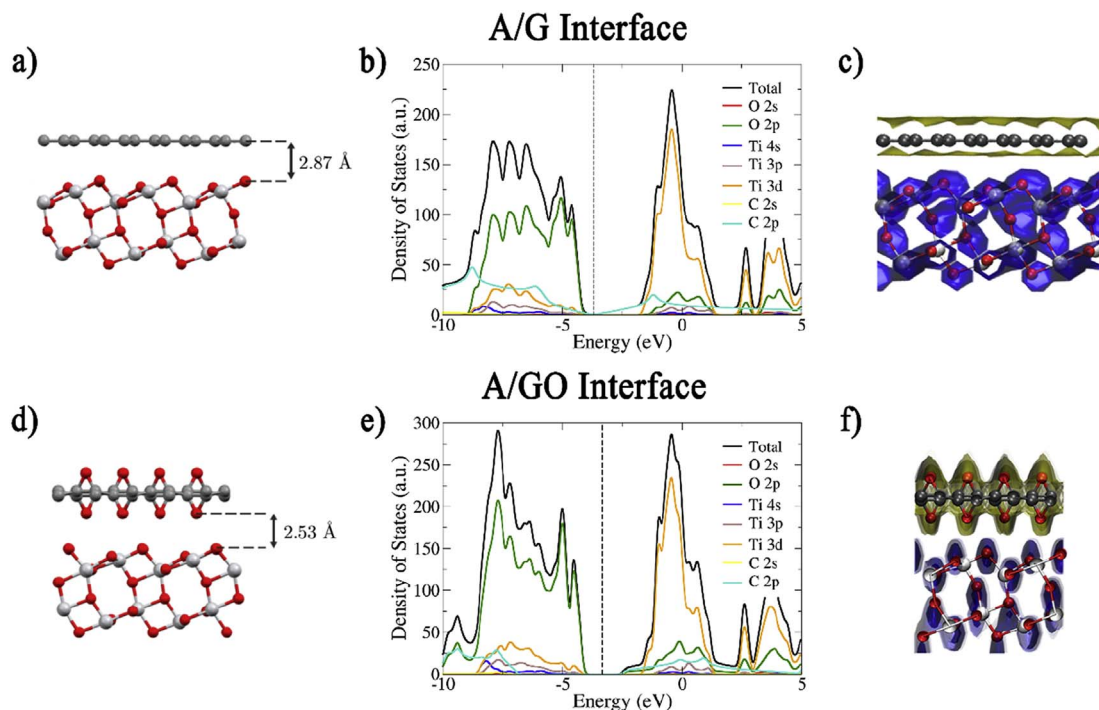
Fig. 1. Optimized geometries (a), (d), total and partial density of states (b), (e) and charge density differences (c), (f) of the interfaces A/G (a)–(c) and A/GO (d)–(f) with an isovalue of 0.0005 e/$\mathring{A}^3$. The vertical dashed lines represent the Fermi energy.

Table 2
Equilibrium distance, adhesion energy, gap energy and G/GO charge per atom calculated for all interfaces.

Interface	Equilibrium distance (Å)	Adhesion energy (eV/C atom)	Gap energy (eV)	G/GO charge (e/atom)
A/G	2.87	−0.028	0	7×10^{-4}
R/G	2.91	−0.021	0	2×10^{-5}
A/GO	2.53	−0.006	1.79	3×10^{-4}
R/GO	2.92	−0.008	1.31	8×10^{-7}

(the broadband at wavenumbers between 500 cm^{-1} and 900 cm^{-1}). Additionally, for the graphene/GO nanocomposites, it is also possible to identify the peaks corresponding to hydroxyl C-OH (1425 cm^{-1}) and epoxy C-O (1150 cm^{-1}) stretching modes [8,28]. These bands are more intense for the TiO$_2$/GO composites but are also observed for the TiO$_2$/G ones, which may be due to the incomplete reduction of the GO during the synthesis of the graphene. The high transmittance band found between 1000 and 450 cm^{-1} shifts to lower wavenumbers for the TiO2/G

3% and TiO2/GO 3% nanocomposites, which indicates the interaction between TiO$_2$ nanoparticles and G/GO, bonds Ti–O–Ti and Ti– O–C.

UV/Vis reflectance of all samples was accessed by DRS and the spectra obtained for pure TiO$_2$, and for TiO$_2$/G 3% and TiO$_2$/GO 3% composites are presented in Fig. 3d. The results show that all the samples reflect approximately 10% of the light when the incident radiation has a wavelength lower than 300 nm. For incident wavelengths in the range 400–800 nm, the reflectance of pure TiO$_2$ is higher than 90%, Further, for this range, TiO$_2$/G and TiO$_2$/GO composites present reflectance values below 30% and 40%, correspondingly. These observations are in good agreement with the dark gray color of the nanocomposites powders and suggest that the these might be photocatalytically active under visible radiation. The band gap of the samples, estimated from DRS spectra by converting the reflectance to Kubelka-Munk units through equation (1), are shown in the inset graph of Fig. 3c.

The values obtained for all the nanocomposites are listed in Table 3 and reveal that the energy gap decreases with increasing wt % of graphene/GO in the composites. Furthermore, TiO$_2$/GO samples show a
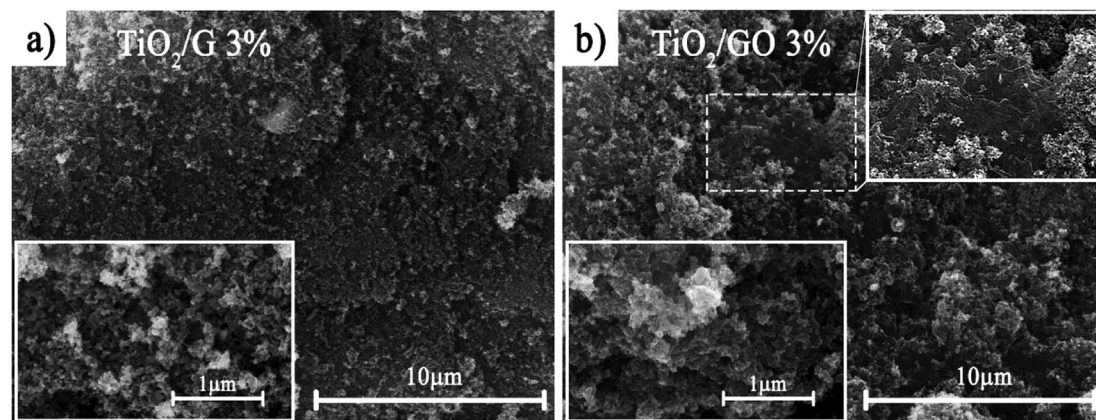

Fig. 2. SEM micrographs, amplified 10 000 (background images) and 100 000 (insets in the lower left corner) times of TiO$_2$/G 3% (a) and TiO$_2$/GO 3% (b) nanocomposites.
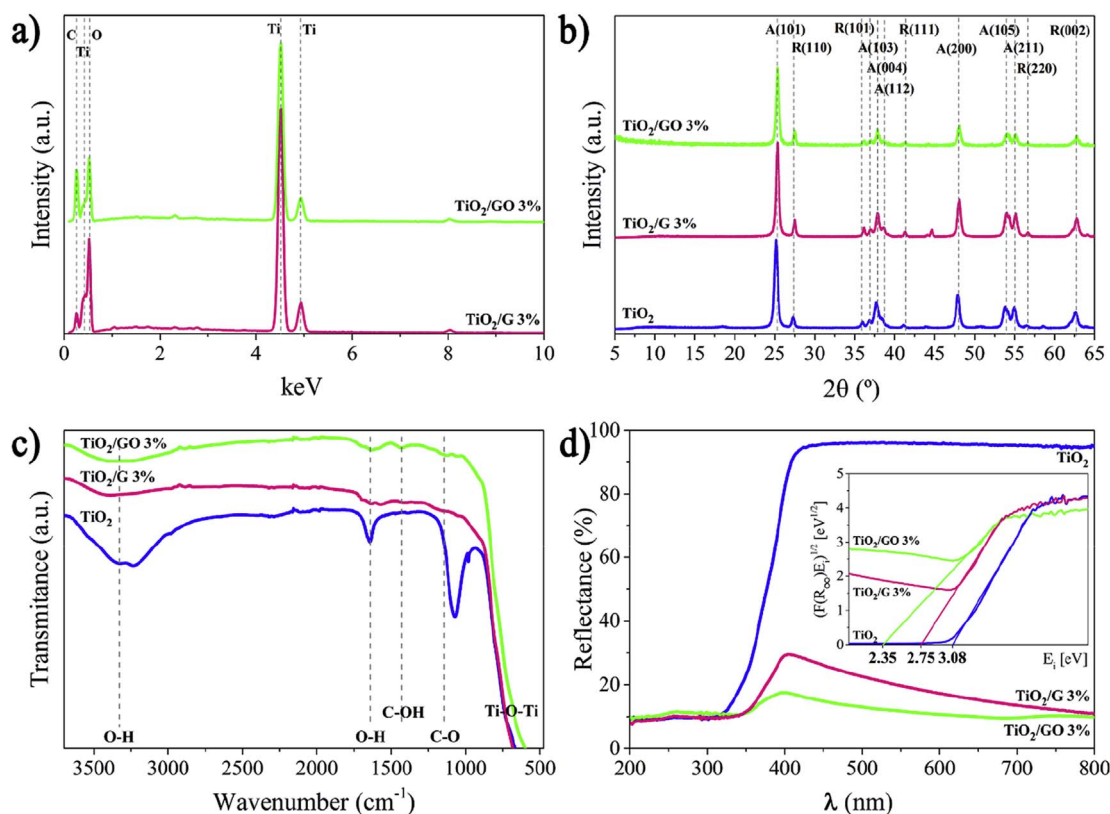
Fig. 3. EDX spectra (a), XRD patterns (b), FTIR-ATR spectra (c) and DRS spectra (d) of pure TiO_2, TiO_2/G 3% and TiO_2/GO 3% composites.

Table 3

- TiO_2 crystalline phases, estimated from XRD spectra, and gap energies, assessed from DRS spectra, of the produced samples.

Sample	TiO_2 crystalline phases		Gap energy (eV)
	%Anatase	%Rutile	
TiO_2	81.6	18.4	3.08
TiO_2/G 0.5%	76.2	23.8	2.94
TiO_2/G 1%	75.9	24.1	2.94
TiO_2/G 1.5%	76.3	23.7	2.89
TiO_2/G 3%	75.3	24.7	2.75
TiO_2/GO 0.5%	75.2	24.8	2.80
TiO_2/GO 1%	73.8	26.2	2.64
TiO_2/GO 1.5%	75.6	24.4	2.53
TiO_2/GO 3%	77.2	22.8	2.35

lower band gap (comprised between 2.35 eV and 2.80 eV, depending on the GO content) than the TiO_2/G ones (between 2.75 eV and 2.94 eV) and, in both cases, these values are inferior to pure TiO_2 (3.08 eV).

The BET specific surface area (S_{BET}) of TiO_2 and GO/TiO_2 samples (0.5, 1, and 3%) was also assessed (supplementary material – Table 2). The results show that the S_{BET} increases with increasing amount of GO. As G is obtained from GO, values for the G/TiO_2 nanocomposites should reflect the same trend.

6.1. Photocatalytic experiments

The investigation of the photocatalytic activity of composites TiO2/G and TiO2/GO under UV radiation through the degradation of MB and CIP aqueous solutions, at room temperature. The assessment of pollutants concentration by monitoring the values of the maximum UV–Vis absorbance peaks for 60 min. For both solutions, the results obtained using pure TiO_2 and different nanocomposites with G and GO are plotted in Fig. 4. The degradation kinetics for all the samples are shown

in supplementary material (Figs. S2 and S3). The apparent reaction rate (k), calculated from the slope of the exponential curve of the concentration plot, and the removal efficiency (both in the UV irradiation period) for all samples are listed in Table 4.

Before the photocatalytic activity tests, a systematic study was performed to the adsorption process (Supplementary material, Fig. S4), confirming the complete saturation of the nanocomposites in the first ≈ 10 min in the dark with the MB solution, under mechanical agitation. For the photocatalytic assays, 30 min in the dark for adsorption-desorption were used to assure a complete saturation of the nanocomposites. Concerning the photocatalytic tests (Fig. 4) large adsorption of MB dye onto the nanoparticles surface was observed during these 30 min, for nanocomposites with higher concentrations of G and GO. Moreover, TiO_2/GO nanocomposites showed higher adsorption of MB than the TiO_2/G ones. For the TiO_2/GO 3% sample, most of the dye was adsorbed onto the catalyst in the equilibration step which prevented the measurement of its photocatalytic activity. The enhanced adsorption of MB is justified by the fact that it is a cationic dye and so it is positively charged in solution. In turn, the presence of carboxylic moieties on the GO surface will favor the electrostatic interaction between the dye and the catalyst surface. A similar but less marked behavior was observed with the CIP solution (Fig. 4b), as CIP showed a lower affinity for the nanocomposites than the MB. This can be rationalized as CIP is also charged in solution but zwitterionic [29]. It is to notice that the increasing adsorption capability of the nanocomposites with increasing amounts of GO and G, is correlated with the corresponding higher specific surface areas (S_{BET}).

Regarding the degradation of MB, the period under UV irradiation (from 0 to 60 min), nanocomposites show a higher photocatalytic performance than pure TiO_2, with larger concentrations of G or GO contributing to the faster degradation of the dye (Table 4). The only exception was the TiO_2/GO 1% composite that presented the lowest rate of degradation (0.064 min^{-1}). For all the tested nanocomposites, MB was fully degraded after ≈ 30 min under UV irradiation.
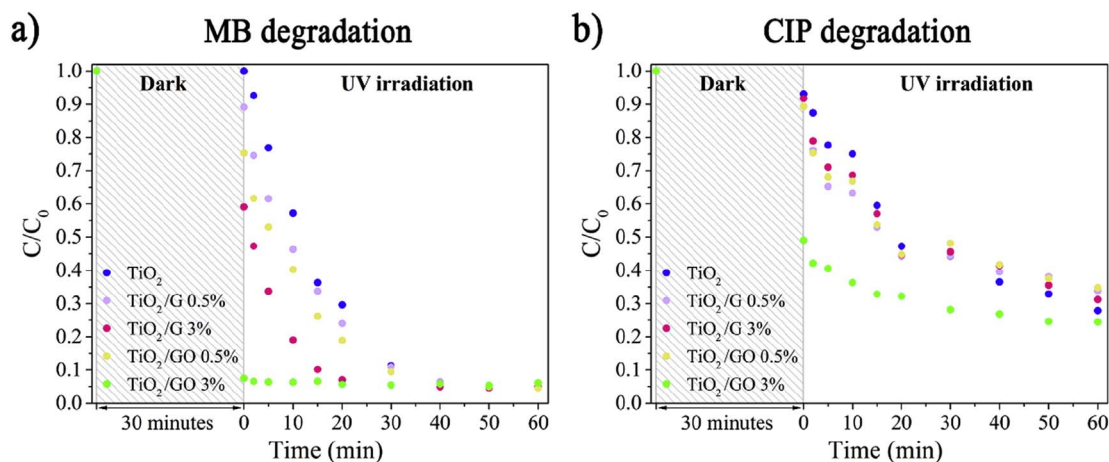
Fig. 4. Photocatalytic degradation of (a) MB and (b) CIP under UV-light irradiation using pure TiO_2, TiO_2/G 0.5%, TiO_2/G 3%, TiO_2/GO 0.5% and TiO_2/GO 3% nanocomposites.

Table 4

First-Order Reaction Rate Constants, k, and Photocatalytic Degradation Efficiencies of all the Samples, Determined After the Degradation Tests of MB and CIP Solutions, Carried Out Under 60 Minutes of UV Irradiation and 180 Minutes of Visible Light Irradiation.

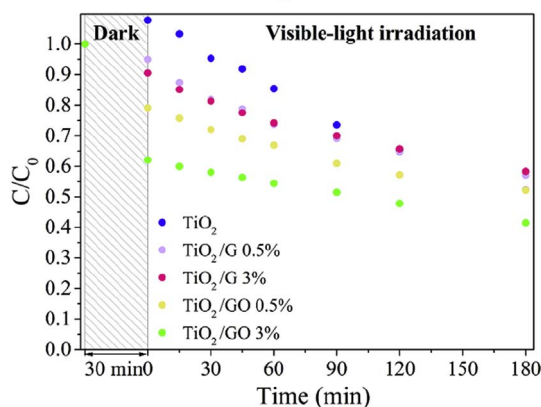| Sample	UV irradiation				Visible light irradiation	
	MB degradation		CIP degradation		CIP degradation	
	k (min^{-1})	%	k (min^{-1})	%	k (min^{-1})	%
TiO_2	0.070	95.23	0.022	70.04	0.004	51.62
TiO_2/G 0.5%	0.088	94.38	0.014	58.66	0.003	39.94
TiO_2/G 1%	0.105	95.08	0.014	66.48	0.002	32.51
TiO_2/G 1.5%	0.121	94.79	0.015	63.22	0.003	36.37
TiO_2/G 3%	0.160	91.69	0.016	65.99	0.002	35.58
TiO_2/GO 0.5%	0.089	93.85	0.013	61.01	0.002	34.14
TiO_2/GO 1%	0.064	91.64	0.014	61.09	0.003	42.99
TiO_2/GO 1.5%	0.115	85.97	0.014	64.84	0.003	37.75
TiO_2/GO 3%	–	–	0.010	50.08	0.002	33.04

Fig. 5. Photocatalytic degradation of CIP under visible-light irradiation using TiO_2/G (a) and TiO_2/GO (b) nanocomposites with different contents of G/GO.

Photocatalytic tests using CIP solution revealed that the tested nanocomposites are less efficient in degrading this pollutant than the powdered TiO_2 under UV irradiation. Furthermore, it was also observed that the degradation of the CIP was slower than that of the MB: after 60 min of exposure to light, a considerable amount of CIP (between 24% and 35% of the initial concentration) was still present. Moreover, the reaction rates and the photocatalytic degradation efficiencies measured for CIP were similar, irrespectively of the G and GO concentration present in the nanocomposites. The reaction rates of the composites range between 0.010 min^{-1} and 0.016 min^{-1}, and their removal efficiencies range from 50% to 67%.

Furthermore, photocatalytic degradation of the CIP solution was also studied under visible-light irradiation, considering the TiO_2/G and TiO_2/GO nanocomposites. The results obtained are plotted in Fig. 5, and the corresponding values of the reaction rate and removal efficiency are listed in Table 4.

Under these conditions, nanocomposites also present a lower photocatalytic activity than pure TiO_2. In fact, a large amount of CIP (between 32% and 59% of the initial concentration) was measured in the solution after 180 min of irradiation. The values of the reaction rates and removal efficiencies (alike with UV light) were low and similar for both composites studied (TiO_2/G and TiO_2/G) and did not vary significantly for different G and GO contents. In particular, reaction rates of the composites assumed values between 0.002 min^{-1} and 0.003 min^{-1}, while the removal efficiencies after 180 min were comprised between 32.51% and 42.99%.

7. Discussion

In this study, complementary computational and experimental assays were performed to evaluate the photocatalytic efficiency of TiO_2/G and TiO_2/GO nanocomposites.

Through computational modeling, interfaces between a TiO_2 surface slab (both in anatase and in rutile crystal phases) and a G or GO layer were constructed, and their electronic properties were determined. Similar TiO_2/G interface models were previously studied using density functional theory (DFT) by Ferrighi et al. [17] and Li et al. [16] (interfaces between anatase (101) and graphene) and by Du et al. [18] (interfaces between rutile (110) and graphene). In contrast, the use of DFTB method in this work allowed the construction of larger interfaces than the reported by those authors, with a considerably higher number of atoms and, subsequently, being highly commensurable and presenting very low strains. On the other hand, to the best of our knowledge, no studies have addressed the computational modeling of TiO_2/GO interfaces. In this case, it is important to note that there is no unique structure for GO, since the conditions and methods of production influence the number, type and distribution of the functional groups of GO [30,31]. In this work, for simplicity, a model where graphene was completely functionalized with epoxy C-O groups was considered to evaluate the effect of oxidation on the fundamental properties of TiO_2/GO interfaces.

For both A/G and R/G interfaces, the distances measured between the TiO_2 slab and the graphene sheet after geometry optimization agree well with the values reported. In particular, the separation calculated

for the A/G interface was 2.87 Å, while the distances obtained by the previous authors were comprised between 2.51 Å, using an LDA + U functional [16], and 2.84 Å, considering PBE-D2 and B3LYP-D functional [17]. For the R/G interface, the 2.91 Å separation determined in this work is slightly higher than the 2.75 Å measured by Du et al. [18] through LDA. The smallest separation, of 2.53 Å, was obtained for the A/GO interface, while the distance measured between the rutile and the GO in the R/GO interface was 2.92 Å.

Additionally, analysis of the DOS plots obtained for the A/G and R/G interfaces lead to the observation of new energy states, corresponding to C 2p orbitals of the graphene, inside the band gap of the TiO_2 in full accordance with the reported in the literature [16–18]. For these interfaces, transitions from the valence to the conduction bands occur directly from the O 2p and Ti 3d states of the TiO_2 to the C 2p states of the graphene. Similar results were obtained for the A/GO and R/GO interfaces, where the presence of the GO was responsible for the introduction of new C 2p and O 2p energy states immediately below the conduction band of the pure TiO_2. So, transitions between the O 2p and Ti 3d states of the TiO_2 to this new set of states of the GO could lower the excitation energy for these interfaces.

Due to the existence of additional energy states, the band gaps of the interfaces are lower than those of pure TiO_2. In particular, the gaps observed for the A/G and R/G systems were null, although like for graphene, there are a low number of states at the Fermi Energy. The energy gaps calculated for A/GO and R/GO interfaces were equal to 1.79 eV and 1.31 eV, respectively, which would correspond to visible and near-infrared radiation. This means that the photoexcitation of the electrons of the TiO_2/G and TiO_2/GO composites can be improved concerning the one of the TiO_2 under solar irradiation. Experimental measurements, performed by DRS, showed that the band gap of the nanocomposites is lower than the gap of pure TiO_2 but by a smaller factor. A decrease in the gap energy with the increase of the content of G and GO in the composites was also observed and is qualitatively in agreement with the computational calculations. However, the experimental band gap values of the TiO_2/G samples were higher than the gaps estimated for the TiO_2/GO composites, contrary to what derived from the computations. This apparently counter-intuitive observation might be rationalized considering that the graphene used in the composites was obtained by reduction of the GO and the existence of defects/holes in the carbon network structure is likely [32] and may lead to extensive band gap opening.

Furthermore, the charge distribution at the interfaces was also analyzed with computer models which resulted in electrons accumulation in the TiO_2 and hole accumulation in the G and GO layers. This means that there is charge transfer between the TiO_2 slab and the G and GO, resulting in a separation of the charge carriers, which can potentially lead to a reduction of their recombination rate, thus enhancing the mechanism of heterogeneous photocatalysis.

In short, due to their electronic properties, it is expected that the TiO_2/G and TiO_2/GO nanocomposites will possess an enhanced photocatalytic activity, especially under visible-light irradiation, when compared with pure TiO_2. This improvement results from their lower energy gap which can allow the quantitative photoexcitation of electrons with solar radiation. Additionally, the separation of the charge carriers at the interfaces should reduce the electron-hole pair recombination rate, and thus should fundamentally enhance the photocatalytic performance of these materials when compared with pure TiO_2.

In the experimental assays, TiO_2/G and TiO_2/GO nanocomposites degraded MB more efficiently than TiO_2 under UV light, as previously observed by Zhang et al. [12] and Nguyen-Phan et al. [14]. The increase of the photodegradation reaction rates of MB occurred with the increase in G or GO content. For the same content of G and GO, these values were very similar for the TiO_2/G and TiO_2/GO composites. These results are in good agreement with those obtained by Nguyen-Phan et al. [14], who observed that an increase in GO content from 1 to

10 wt % yielded higher degradation rates of the MB. At the same time, these results are also in accordance with the computed electronic properties of these materials.

In contrast with the observations with MB, TiO_2/G and TiO_2/GO nanocomposites presented a lower photocatalytic activity under UV light for CIP degradation than pure TiO_2. Furthermore, for this pollutant, the values of the reaction rate constant and removal efficiency did not change significantly, regardless the different G and GO concentration tested. Analogous results were obtained when these photocatalysts were used to degrade the CIP solution under visible-light irradiation.

Computer modeling addresses the fundamental properties of TiO_2/G and TiO_2/GO interfaces, and the results indicate that the composites should have enhanced photocatalytic properties than pure TiO_2 nanoparticles due to their electronic properties. The experimental results have shown that the photocatalytic efficiency is also strongly dependent on the pollutant molecular properties and chemical structure. According to literature, the compound to degrade also influences the dependence of the photocatalytic activity with the content of G/GO. For example, under UV-light irradiation TiO_2/GO nanocomposites, Nguyen-Phan et al. [14] observed an increase in the degradation rates of the MB with the increase of GO content from 1% to 10%. In contrast, Yadav et al. [33] reported that an increase in wt % of GO from 0.25% to 2% lead to a decrease in the degradation rates of benzene gas.

The well-known adsorption properties of carbonaceous materials (like G or GO) [14,34], our computational results and the efficient MB degradation indicate and support the enhanced photocatalytic properties of the nanocomposites compared with the pristine TiO_2. In this sense, the inefficient degradation of CIP is a consequence of the chemical and molecular properties of this compound, and not due to the catalyst the catalyst. The adsorption of MB and CIP after 30 min in the dark also mirror this idea; it is possible to observe that the adsorption occurred with MB is significantly higher than with CIP. The adsorption process is critical for photocatalysis efficiency, in this way, the low affinity of CIP molecules with the nanocomposites, compromises the adsorption of CIP into the nanocomposite surface and consequently reduces the photocatalytic efficiency. The described low adsorption is even more evident in the G nanocomposites (for MB and CIP degradation), as it becomes more hydrophobic than GO due to the loss of O groups [35].

These results corroborate the idea that the photocatalytic efficiency depends not only on the electronic properties of the used photocatalyst, but it is also highly dependent on the pollutant considered and of its interactions with the catalyst surface.

8. Conclusions

A comprehensive work enclosing a computational study focused on TiO_2/G and TiO_2/GO interfaces, and the experimental photocatalytic performance of these nanocomposites with different contents of G and GO was carried out. Computational results of the fundamental electronic properties of the nanocomposites have shown that these are potentially more efficient than pure TiO_2, due to their lower energy gap and to the existence of a charge separation at the interfaces, which reduces the recombination of electron-hole pairs. The nanocomposites characterization, through SEM, and FTIR confirmed the interaction between TiO_2 nanoparticles and G or GO. Additionally, the reflectance measurements corroborate the computational results, with lower band gaps for the nanocomposites (ranging from 2.94 to 2.35 eV) compared with TiO_2 (3.08 eV). Experimental results revealed that the nanocomposites degrade more efficiently the MB than the TiO_2, but the opposite occurs for CIP. These results indicate that the photocatalytic efficiency depends not only on the properties of the catalyst but also on the compound to degrade and its favorable/unfavorable interactions with the catalytic surface. In this situation, CIP does not have an efficient interaction with the nanocomposite surface, which promotes low adsorption and adverse outcomes for the photocatalytic process.

Therefore, further theoretical and experimental studies are required with different pollutants to fully elucidate the mechanism behind the observed behavior of these composites and to be able to accurately match photocatalyst properties with specific pollutants for an optimized degradation.

Acknowledgments

Appendix A. Supplementary data

Supplementary data related to this article can be found at http://dx.doi.org/10.1016/j.compositesb.2018.03.015.

References

[1] Schwarzenbach R. The challenge of micropollutants in aquatic systems. Sci Technol 2006;313:1072–7. http://dx.doi.org/10.1126/science.1127291.

[2] Muñoz I, Gómez M, Molina-Díaz A, Huijbregts M, Fernández-Alba A, García-Calvo E. Ranking potential impacts of priority and emerging pollutants in urban wastewater through life cycle impact assessment. Chemosphere 2008;74:37–44. http://dx.doi.org/10.1016/j.chemosphere.2008.09.029.

[3] Eckert H, Bobeth M, Teixeira S, Kühn K, Cuniberti G. Modeling of photocatalytic degradation of organic components in water by nanoparticle suspension. Chem Eng J 2015;261:67–75. http://dx.doi.org/10.1016/j.cej.2014.05.147.

[4] Martins PM, Gomez V, Lopes AC, Tavares CJ, Botelho G, Irusta S, et al. Improving photocatalytic performance and recyclability by development of Er-doped and Er/Pr-codoped TiO$_2$/poly(vinylidene difluoride) − trifluoroethylene composite membranes. J Phys Chem C 2014;118:27944–53. http://dx.doi.org/10.1021/jp509294v.

[5] Luo Y, Guo W, Ngo HH, Nghiem LD, Hai FI, Zhang J, et al. A review on the occurrence of micropollutants in the aquatic environment and their fate and removal during wastewater treatment. Sci Total Environ 2014;473–474:619–41. http://dx.doi.org/10.1016/j.scitotenv.2013.12.065.

[6] Mills A, Le Hunte S. An overview of semiconductor photocatalysis. J Photochem Photobiol Chem 1997;108:1–35. http://dx.doi.org/10.1016/S1010-6030(97)00118-4.

[7] Anandan S, Narasinga Rao T, Sathish M, Rangappa D, Honma I, Miyauchi M. Superhydrophilic graphene-loaded TiO$_2$ thin film for self-cleaning applications. ACS Appl Mater Interfaces 2013;5:207–12. http://dx.doi.org/10.1021/am302557z.

[8] Almeida N, Martins P, Teixeira S, Lopes da Silva J, Sencadas V, Kühn K, et al. TiO$_2$/graphene oxide immobilized in P(VDF-TrFE) electrospun membranes with enhanced visible-light induced photocatalytic performance. J Mater Sci 2016;51:6974–86. http://dx.doi.org/10.1007/s10853-016-9986-4.

[9] Kozlova EA, Vorontsov AV. Noble metal and sulfuric acid modified TiO$_2$ photocatalysts: mineralization of organophosphorous compounds. Appl Catal B Environ 2006;63:114–23. http://dx.doi.org/10.1016/j.apcatb.2005.09.020.

[10] Marschall R, Wang L. Non-metal doping of transition metal oxides for visible-light photocatalysis. Catal Today 2014;225:111–35. http://dx.doi.org/10.1016/j.cattod.2013.10.088.

[11] Liu J, Wang L, Tang J, Ma J. Photocatalytic degradation of commercially sourced naphthenic acids by TiO$_2$-graphene composite nanomaterial. Chemosphere 2016;149:328–35. http://dx.doi.org/10.1016/j.chemosphere.2016.01.074.

[12] Zhang H, Lv X, Li Y, Wang Y, Li J. P25-graphene composite as a high performance photocatalyst. ACS Nano 2009;4:380–6.

[13] Calza P, Hadjicostas C, Sakkas VA, Sarro M, Minero C, Medana C, et al. Photocatalytic transformation of the antipsychotic drug risperidone in aqueous media on reduced graphene oxide — TiO$_2$ composites. Appl Catal B Environ 2016;183:96–106. http://dx.doi.org/10.1016/j.apcatb.2015.10.010.

[14] Nguyen-Phan T, Pham VH, Shin EW, Pham H, Kim S, Chung JS, et al. The role of graphene oxide content on the adsorption-enhanced photocatalysis of titanium dioxide/graphene oxide composites. Chem Eng J 2011;170:226–32. http://dx.doi.org/10.1016/j.cej.2011.03.060.

[15] Wang P, Wang J, Ming T, Wang X, Yu H, Yu J, et al. Dye-sensitization-induced visible-light reduction of graphene oxide for the enhanced TiO$_2$ photocatalytic performance. ACS Appl Mater Interfaces 2013;5:2924–9. http://dx.doi.org/10.1021/am4008566.

[16] Li X, Gao H, Liu G. A LDA + U study of the hybrid graphene/anatase TiO$_2$ nanocomposites: interfacial properties and visible light response. Comput Theor Chem 2013;1025:30–4. http://dx.doi.org/10.1016/j.comptc.2013.10.006.

[17] Ferrighi L, Fazio G, Valentin C. Charge carriers separation at the graphene/(101) anatase TiO$_2$ interface. Adv Mater Interfaces 2016;3:1–7. http://dx.doi.org/10.1002/admi.201500624.

[18] Du A, Ng H, Bell NJ, Zhu Z, Smith SC. Hybrid graphene/titania nanocomposite: interface charge transfer, hole-doping and sensitization for visible light response. J Phys Chem Lett 2011;2:894–9. http://dx.doi.org/10.1021/jz2002698.

[19] Aradi B, Hourahine B, Frauenheim T. DFTB +, a sparse matrix-based implementation of the DFTB method. J Phys Chem 2007;111:5678–84.

[20] Koskinen P, Mäkinen V. Density-functional tight-binding for beginners. Comput Mater Sci 2009;47:237–53. http://dx.doi.org/10.1016/j.commatsci.2009.07.013.

[21] Elstner M, Seifert G. Density functional tight binding. Philos Trans R Soc 2014;372:20120483 https://doi.org/10.1098/rsta.2012.0483.

[22] Hummers W, Offeman R. Preparation of graphitic oxide. J Am Chem Soc 1958;80. http://dx.doi.org/10.1021/ja01539a017. 1339–1339.

[23] Goncalves G, Marques P, Granadeiro C, Nogueira H, Singh M, Grácio J. Surface modification of graphene nanosheets with gold nanoparticles: the role of oxygen moieties at graphene surface on gold nucleation and growth. Chem Mater 2009;21:4796–802. http://dx.doi.org/10.1021/cm901052s.

[24] Torrent J, Barrón V. Diffuse reflectance spectroscopy. Meth Soil Anal Soil Sci Soc Am 2008:367–85.

[25] Hoffmann M, Martin S, Choi W, Bahnemann D. Environmental applications of semiconductor photocatalysis. Chem Rev 1995;95:69–96. http://dx.doi.org/10.1021/cr00033a004.

[26] Dufour F, Pigeot-Remy S, Durupthy O, Cassaignon S, Ruaux V, Torelli S, et al. Morphological control of TiO$_2$ anatase nanoparticles: what is the good surface property to obtain efficient photocatalysts? Appl Catal B Environ 2015;174–175:350–60. http://dx.doi.org/10.1016/j.apcatb.2015.03.013.

[27] Blanton T, Majumdar D. Characterization of x-ray irradiated graphene oxide coatings using x-ray diffraction, x-ray photoelectron spectroscopy, and atomic force microscopy. JCPDS Int Cent Differ Data 2013:116–22.

[28] Wang P, Wang J, Wang X, Yu H, Yu J, Lei M, et al. One-step synthesis of easy-recycling TiO$_2$-rGO nanocomposite photocatalysts with enhanced photocatalytic activity. Appl Catal, B 2013;132–133:452–9. http://dx.doi.org/10.1016/j.apcatb.2012.12.009.

[29] Garrido JMPJ, Melle-Franco M, Strutyński K, Borges F, Brett CMA, Garrido EMPJ. β–Cyclodextrin carbon nanotube-enhanced sensor for ciprofloxacin detection. J Environ Sci Health Part A 2017;52:313–9. http://dx.doi.org/10.1080/10934529.2016.1258864.

[30] Nasehnia F, Lima SM, Seifi M, Mehran E. First principles study on optical response of graphene oxides: from reduced graphene oxide to the fully oxidized surface. Comput Mater Sci 2016;114:112–20. http://dx.doi.org/10.1016/j.commatsci.2015.12.010.

[31] Putri LK, Tan LL, Ong WJ, Chang WS, Chai SP. Graphene oxide: exploiting its unique properties toward visible-light-driven photocatalysis. Appl Mater Today 2016;4:9–16. http://dx.doi.org/10.1016/j.apmt.2016.04.001.

[32] Bagri A, Mattevi C, Acik M, Chabal YJ, Chhowalla M, Shenoy VB. Structural evolution during the reduction of chemically derived graphene oxide. Nat Chem 2010;2:581–7. http://dx.doi.org/10.1038/nchem.686.

[33] Yadav H, Kim J. Solvothermal synthesis of anatase TiO$_2$-graphene oxide nanocomposites and their photocatalytic performance. J Alloy Comp 2016;688:123–9. http://dx.doi.org/10.1016/j.jallcom.2016.07.133.

[34] Bai H, Zhou J, Zhang H, Tang G. Enhanced adsorbability and photocatalytic activity of TiO$_2$-graphene composite for polycyclic aromatic hydrocarbons removal in aqueous phase. Colloids Surfaces B Biointerfaces 2017;150:68–77. http://dx.doi.org/10.1016/j.colsurfb.2016.11.017.

[35] Faraldos M, Bahamonde A. Environmental applications of titania-graphene photocatalysts. Catal Today 2017;285:13–28. http://dx.doi.org/10.1016/j.cattod.2017.01.029.